Environmental Science Nano

Chronic exposure to complex metal oxide nanomaterials induces production of reactive oxygen species in bacteria

Journal:	*Environmental Science: Nano*
Manuscript ID	EN-ART-12-2022-001144.R1
Article Type:	Paper

This study explores the impact of engineered nanomaterials, widely utilized as cathode battery materials, on the environmentally relevant bacteria *Shewanella oneidensis*. Industrial scale manufacture of nanomaterials eventually leads to their accumulation in the environment. Understanding the toxicity of nanomaterials to environmental organisms will direct researchers to create less toxic compositions of nanomaterials or aid in the development of safer use and disposal regulations. In this study, nanomaterials lead to generation of toxic reactive oxygen species, creating random mutations in the bacterial genome, changing bacterial physiology, and resulting in the evolution of resistance to antibiotics. These changes can impair native bacterial functionality and the acquired mutations could potentially be horizontally transferred to other organisms, increasing the incidences of antibiotic resistance in multiple bacterial species.

Chronic exposure to complex metal oxide nanomaterials induces production of reactive oxygen species in bacteria

Deepti Sharan[1], Daniel Wolfson[2], Curtis M. Green[3,4], Paul Lemke[2], Alessandra G. Gavin[1], Robert J. Hamers[3], Z. Vivian Feng[2,5], Erin E. Carlson[1,6,7,*]

[1]Department of Chemistry, University of Minnesota, 225 Pleasant St. SE, Minneapolis, MN, 55454, United States
[2]Department of Chemistry, Augsburg University, 2211 Riverside Ave, Minneapolis, MN 55454, United States
[3]Department of Chemistry, University of Wisconsin-Madison, 1101 University Avenue, Madison, WI 53706, United States
[4]Process and Analytical Development, MilliporeSigma, 645 Science Drive, Madison, WI 53711, United States
[5]Council on Science and Technology, Princeton University, 1 Washington Rd, Princeton, NJ 08544, United States
[6]Department of Medicinal Chemistry, University of Minnesota, 208 Harvard Street SE, Minneapolis, MN 55454, United States
[7]Department of Biochemistry, Molecular Biology, and Biophysics, University of Minnesota, 321 Church St SE, Minneapolis, MN 55454, United States
*Corresponding author: carlsone@umn.edu

Abstract

Use of complex metal oxide nanoparticles has drastically risen in recent years, especially due to their utility in electric vehicle batteries. However, use of these materials has outpaced our understanding of how they might affect environmental organisms, which they could encounter through release during manufacture, use, and disposal. In particular, little is known about the effects of chronic exposure to complex metal oxide nanoparticles. Here, we have focused on an environmentally relevant bacterial species, *Shewanella oneidensis,* which is ubiquitous in nature and responsible for bioremediation of heavy metals and assessed the toxic effects of nanoscale lithiated nickel manganese cobalt oxide (NMC), which is an emerging battery cathode material for electronic devices. We previously reported that chronic exposure of *S. oneidensis* to NMC results in the emergence of an adaptive phenotype where the bacteria are able to tolerate otherwise lethal concentrations of NMC. In the present study,

we aim to investigate the role of reactive oxygen species (ROS) and changes in phenotype of the NMC-adapted bacterial population. We found that NMC-exposed bacteria possess ROS-containing membrane vesicles, as well as an increased propensity to generate random DNA mutations and harbor other DNA damage. Thus, our data indicate substantial genetic-level variation in bacteria that results from chronic exposure to toxic complex metal oxide nanomaterials.

Introduction

Emerging technologies in several fields like energy, pharmaceuticals, catalysis, and textiles have increased demand for highly efficient nanomaterial-based systems, which are cost effective and easy to use. Focusing on the energy front, it has been estimated that the use of nanomaterial-based systems will increase by 2050 due to the demand for more electric vehicles. Recent advances have made nanoscale lithiated nickel manganese cobalt oxide ($Li_xNi_yMn_zCo_{1-y-z}O_2$, $0 < x,y,z < 1$, abbreviated as NMC) a viable option as a highly efficient battery cathode material(1-3). NMC has a layered structure that is similar to nanoscale lithium cobalt oxide (LCO)(4) and has gained interest due to its superior ability to transport lithium ions to provide better conduction, and the reduced impact of mechanical stress during lithium intercalation and deintercalation(5-7). As NMC has huge commercial benefits, its large-scale production and use also increases the likelihood that it will enter the natural environment during manufacturing, usage, and waste disposal. The costs and energy requirements for recycling lithium ion- or NMC-based battery materials are high and large quantities of these materials go into landfills. Nickel, manganese, cobalt, and lithium ions often leak from the buried batteries, which ultimately contaminate land, ground water, and other water bodies. As such, it is critical for us to understand the effects of NMC on the ecosystem and organisms in the environment. We and others have previously reported that NMC exhibits toxic effects to many species including

bacteria and aquatic organisms (8-11). Here, we investigate the roles of reactive oxygen species (ROS), DNA damage, and mutation frequency in the response of the bacteria *Shewanella oneidensis* to NMC.

NMC nanoparticles have sheet-like morphology (12) with an average size of 84±22 nm measured along the basal plane (10). Full characterization details for NMC used in these studies is provided in the Supporting Information. An electric vehicle typically has 40-50 kg of NMC nanomaterial in the battery pack (7). Thus, improper materials disposal could result in the release of tens of kilograms of NMC. Indeed, leachate from landfills containing lithium ion batteries has been found to have toxic levels of various heavy metals linked to battery materials (59). The concentration of these materials in the environment is highly variable, but our previous work has shown that concentrations of > 25 mg/L are toxic to bacterial cells (12).

NMC nanomaterials have toxic effects on growth of the environmentally-relevant bacterial species *Shewanella oneidensis* MR-1. *S. oneidensis* is a Gram-negative bacterium that is ubiquitously present in the environment including soil, sediment and aquatic systems and possesses metal cycling and remediation properties. Reports suggest that in addition to being toxic, NMC decreases cellular respiration in bacteria, as measured by oxygen consumption and also leads to DNA damage within eight hours of exposure in *S. oneidensis*, as studied by the comet assay and high-resolution DNA adductomics (10, 13). Interestingly, NMC nanoparticles cannot enter the bacteria as determined by high resolution scanning electron microscopy and transmission electron microscopy and are believed to exert toxic effects by their presence in the vicinity of the cells (10). NMC is transformed in liquid as shown by surface composition studies using XPS and metal dissolution by ICP-OES. NMC undergoes incongruent dissolution resulting in metal ion release and ROS generation (10). Relatedly, H_2O_2 generation from freshly suspended lithium cobalt oxide nanomaterials (similar to NMC, but without Ni and Mg) has been shown to led to ROS damage in bacterial cells (14). H_2O_2 is cell permeable and is

known to itself cause an increase in cellular production of other ROS, such as hydroxyl radicals, in bacteria.

We previously reported that chronic exposure to NMC leads to the development of resistance (or adaptation) in bacteria where these organisms can grow in the presence of NMC concentrations that were toxic in earlier exposures(12). The ion equivalents of NMC (the ions released from NMC during 72 hr of exposure) were not as toxic as the particles themselves, indicating an effect that is specific to nanoparticle exposure(12). We found that during the process of adaptation to NMC, a portion of the bacterial population become filamented and can increase to 10-30 μm in length (wild-type 2-3 μm) with a minor population being elongated to 80-100 μm(12). This extreme filamentation was not observed upon exposure to the ion equivalents of NMC, again indicating a nanoparticle-specific consequence.

Filamentation is a common bacterial response to stress from a variety of conditions such as DNA damage(15), starvation(16-18), exposure to antibiotics(19, 20), changes in pH, low temperature, host immune response, or onset of the SOS response(21-23). The SOS response is an inducible global response triggered in bacteria upon DNA damage where cell division is arrested and the expression of several DNA repair proteins is induced to promote DNA integrity for improved survival at the cost of increased mutagenesis. While filamentation leads to division arrest, it also allows the cells to replicate and repair DNA damage to ensure that a repaired chromosome is passed to progeny. This process has largely been studied in *Escherichia coli* where division is halted until the DNA is repaired, which is sensed by SulA, a protein that remains bound to the essential cell division protein, FtsZ, until repair has been completed(15, 24, 25). Bacterial filamentation has also been correlated with the SOS response, reactive oxygen species (ROS),(26) and DNA damage.

We postulated that ROS may be a critical player in the filamentation of *S. oneidensis* upon NMC exposure as ROS may be generated by interaction of surface groups of NMC with

molecular oxygen, which then participates in subsequent reactions to form additional ROS species(27). Thus, dissolution of metal-containing nanomaterials could be one cause of ROS formation,(28) which has been correlated with their toxicity(29-34). Most aerobically respiring organisms have built-in mechanisms to maintain redox balance including detoxification enzymes such as catalase, peroxidase, glutathione reductase, superoxide dismutase, and thiol metabolites. However, these systems can be overwhelmed when the cell encounters high concentrations of exogenous ROS, resulting in its accumulation and oxidative stress. Ultimately, widespread damage can result, such as protein and lipid damage, disruption of metal homeostasis, DNA strand breakage, and single nucleotide modifications(13, 14, 35-37). The present study examines the roles of ROS in the response of *S. oneidensis* to NMC with focus on filamentation, DNA damage, and mutation.

Experimental Section

Bacterial strain and growth conditions

Shewanella oneidensis MR-1 (ATCC BAA1096) was grown on Luria Broth (LB) agar plates at 30 ºC for 16-20 h. Liquid cultures were grown in minimal medium (MM) containing 88.1 mM Na_2HPO_4, 50.5 mM $CaCl_2$, 11.6 mM NaCl, 10 mM HEPES, 4.0 mM KCl, 2.8 mM NH_4Cl, 2.8 mM Na_2SO_4, 1.4 mM $MgCl_2$ and 100 mM sodium lactate. A single colony was picked from the plate and inoculated into 5 mL of MM for primary cultures and grown at 30 ºC, shaking at 250 rpm, for 24 h. Overnight cultures were diluted to an optical density (OD_{600}) of 0.1 at 600 nm (GENESYS 20 spectrophotometer, ThermoFisher Scientific) for sub-culturing/passages. The first sub-culture was performed with a 10% dilution (1:10 v/v) of the overnight diluted culture in fresh MM and is referred to as “passage A”. After 72 h of growth, the culture was again diluted to 0.1 OD and sub-cultured into passage B. This was repeated until passage D. All the samples were prepared in triplicate and bacterial growth assessed by measuring OD_{600}.

Nanoparticle addition

NMC nanoparticles were synthesized as previously published(10, 12). When needed, a fresh stock of dispersed NMC solution was prepared at the concentration of 2 mg/mL in minimal media with sonication for 10 min. The dispersed NMC was added to the cultures (25 mg/L) 10 h after inoculation for the first passage (passage A). For subsequent passages, NMC was added at the time of bacterial inoculation as in the previous study(12). Similarly, ion equivalents were prepared from fresh stock solutions of LiOH, $NiCl_2$, $MnSO_4$, and $CoCl_2$ and added to the cultures to achieve a final concentration as present following dissolution of NMC over 72 h in minimal media(12).

ROS estimation using DCF-DA dye

ROS was measured using a cell-permeant dye 2',7'-dichlorodihydrofluorescein diacetate (H_2DCFDA) or DCFDA dye (ThermoFischer Scientific/Invitrogen, D399). NMC-exposed, Ion eqv.-exposed and unexposed bacterial samples were stained by adding 5 µM final concentration to 200 µL of culture in Eppendorf tubes, mixed by brief vortex (~2 sec) and incubated in the dark for 30 min at room temperature. For microscopy, 5-10 µL stained culture, unfixed, was spread on a glass slide, covered with coverslip, and imaged under fluorescence microscope (Olympus) with 100X magnification and 1.4 numerical aperture. Brightfield and fluorescent images were taken using the brightfield channel and FITC fluorescence channel, respectively, at fixed exposure time of 500 ms. For plate reader-based assay, 200 µL DCFDA-stained cultures were transferred to a black 96-well flat bottom black (Greiner) and read in a plate reader (Tecan) at ex/em of 488/535 nm. The fluorescence readings were blank subtracted as well as corrected for the bacterial count obtained using colony forming units (CFU) for each sample. The data was analyzed and plotted using GraphPad Prism software. For flow cytometry, the samples were prepared in larger volume by aliquoting 1 mL from the cultures directly into the flow cytometry tubes and stained with DCFDA at the final concentration of 5 µM and

incubated at room temperature for 30 min in the dark. An autofluorescence control was also taken for all the samples without addition of the DCFDA dye. Samples were analyzed by BD LSR II H4710 flow cytometer with a 488 nm excitation laser (20 mW blue laser), 525/50 BP emission filter with FITC (488 E) settings and 10,000 events were captured at medium flow rate for all the samples. A P1 gate was constructed by considering the spread of the population in the unstained samples (without the addition of DCFDA dye) and these samples were termed as autofluorescence controls. This P1 gate was placed in such a way to avoid maximum cells from all the autofluorescence samples. Thus, only the cells with fluorescence in DCFDA dye stained samples can be monitored in P1 gate. Data acquisition and data analysis were performed using BD FACSDiva™ software.

Hydroxyl radical levels by HPF dye

Hydroxyphenyl fluorescein, also known as 2-[6-(4′-hydroxy)phenoxy-3H-xanthen-3-on-9-yl]benzoic acid or HPF (Sigma-Aldrich, H4290) was used for the estimation of hydroxyl radicals in the samples. Unexposed bacterial cultures, as well as those exposed to NMC or ion eqv., were aliquoted in fresh Eppendorf tubes, 200 µL of all samples in triplicate and stained with HPF at the final concentration of 5 µM for 15 min in the dark at room temperature. The samples were transferred to a black 96-well flat bottom black (Greiner) and read in a plate reader (Tecan) at ex/em of 490/520 nm. The fluorescence readings were blank subtracted from the respective MM blank, NMC in MM blank or ion eqv. in MM blank, as well as corrected for the bacterial count obtained using colony forming units (CFU) for each sample. The data were analyzed and plotted using GraphPad Prism software. For flow cytometry analysis, 1 mL of all the samples was aliquoted directly into the flow cytometry tubes and stained with HPF at the final concentration of 5 µM and incubated at room temperature for 15 min in the dark. An autofluorescence control was taken for all the samples without addition of HPF dye. This was used the set a gate outside the autofluorescence signals in FSC/SSC to get the fluorescence-

positive samples in the gated population. The samples were analyzed by BD LSR II H4710 flow cytometer with a 488 nm excitation laser (20 mW blue laser), 525/50 BP emission filter with FITC settings and 10,000 events were captured at medium flow rate for all the samples. P1 gate was constructed as described in previous paragraph. Data acquisition and data analysis were performed using BD FACSDiva™ software.

Amplex Red assay for H_2O_2 concentration quantification

Amplex Red assay kit (Invitrogen, A22188) was used to estimate the H_2O_2 concentration of the NMC/ion eqv.-exposed and unexposed cultures. All reagents were prepared as per manufacturer's protocol with the stock concentrations of 10 mM Amplex red reagent and 10 U/ml HRP solution. Standards for H_2O_2 were also prepared from 0.1 μM to 10 μM in order to generate a standard curve to calculate the concentrations of H_2O_2 in the samples. A H_2O_2 scavenger, dimethyl thiourea-containing controls were also prepared to ensure the presence of H_2O_2 in the samples. From the NMC/ion eqv.-exposed and unexposed cultures, 50 μL were transferred to individual wells in 96-well black plate as well as the H_2O_2 standard solutions were also added to different wells. To all the samples, 50 μL of Amplex Red/HRP working solution was added to attain a final working concentration of 100 μM Amplex Red reagent and 0.2 U/ml HRP, followed by incubation at room temperature for 30 min in the dark. The fluorescence readings were taken using a plate reader (Tecan) at ex/em of 530/590 nm every 15 min over 1 hr. The readings thus obtained were blank subtracted and the limit of detection and limit of quantitation were calculated from the triplicate readings. Following the blank subtraction, the H_2O_2 standard curve was plotted using GraphPad Prism and the straight-line equation was obtained using the linear regression settings. These values were used to calculate the concentration of H_2O_2 present in the samples. As Amplex Red reagent cannot enter the bacterial cells, these values indicate the presence of H_2O_2 in the total volume of the samples, which has been used for the comparison among different samples. Concentration of H_2O_2

released per cell has also been calculated using the CFU count for all the culture samples. Abiotic NMC-only, as well as ion-only controls in minimal media were also used to estimate the H_2O_2 release from NMC/ion eqv. in minimal media.

Membrane staining

Bacterial lipid membrane was visualized using commercially available fluorescent dye FM™ 4-64 or (N-(3-Triethylammoniumpropyl)-4-(6-(4-(Diethylamino) Phenyl) Hexatrienyl) Pyridinium Dibromide), (Invitrogen, T13320). From the NMC/ion eqv.-exposed and unexposed cultures, 200 µL of culture was aliquoted and 2 µL of FM4-64 dye was added to samples to attain a concentration of 1 µg/mL, vortexed briefly. These samples were incubated at room temperature for 15 min in the dark. From the stained samples, 10 µL was spread on a glass slide, covered with a coverslip and fluorescence imaged using the TRITC channel with ex./em. of 544/570 nm on an inverted microscope (Olympus) with 100 X magnification and 1.4 numerical aperture.

Cell wall peptidoglycan staining

A fluorescent D-amino acid (FDAA) was used to image the peptidoglycan layer in bacterial cells and vesicles. RADA (Orange-red TAMRA-based FDAA, R&D systems-biotechne, cat. No. 6649) was used at the final concentration of 1 µM and added to 200 µL of culture and kept at room temperature for 15 min in the dark. Cells were imaged as described previously during FM4-64 staining. Ten µL of the stained cultures was spread on a glass slide, covered with a coverslip and fluorescence imaged using the TRITC channel on an inverted microscope (Olympus) with 100 X magnification and 1.4 numerical aperture.

Live cell time-lapse imaging

Live cell imaging was performed on 1.5% agarose pads prepared with minimal media using a glass bottom µ-dish, 35 mm, #1.5H (170 µm +/- 5 µm) D 263 M Schott glass, sterilized (Ibidi, Cat. # 81158). Bacterial cultures at 72 h were used for imaging, 100 µL culture was evenly

spread on the sterile glass bottom dish, by tilting or spotting. A 1.5% low melting temperature agarose solution was made in minimal media and poured over the 100 µL culture in the glass bottom dish. This was solidified at room temperature for 30 min. Cells were imaged under the microscope with 100 X magnification, equipped with an environmental chamber to maintain a temperature of 30 ºC. Images were captured at regular intervals of 5 min to generate a time-lapse combined image.

CFU estimation

For all experiments, 20 µL of the cultures were mixed with 180 µL MM. This was considered as -1 dilution. From this sample, 100 µL was taken into a fresh tube and 900 µL MM added and considered as the -2 dilution and likewise serially diluted to a -6 dilution. From all the dilutions, 10 µL was spotted on LB agar plates, dried, and incubated at 30 ºC for 12-16 h. Separated colonies were counted (not merged or joined), ranging from 1-30. Colonies were also matched with the immediate next dilution for consistency of the counting. Colony counts were back calculated to determine the number of the cells per sample.

Comet assay

Single cell gel electrophoresis analysis, a.k.a., comet assay, was conducted on *S. oneidensis* cells from multiple passages upon re-exposure to NMC, following published protocols(13, 14). Briefly, bacterial cells were grown and exposed to NMC or NMC + thiourea for 72 h at each passage. Forty microliters of a bacterial suspension and low-melting agarose (LMA) mixture (1:10 ratio) were placed in a well of a Comet assay slide (Travigen®) and spread evenly. Upon solidifying, an LMA layer containing 0.5% lysozyme was placed on top and solidified. The slide was incubated at 30 ºC for 30 min, and immersed in a lysing solution containing 2.5 M NaCl, 100.0 mM EDTA, 10.0 mM Tris-HCl, 1% sodium N-lauryl sarcosine, 0.6% Triton® X-100 at pH 10.0 for 1 h, followed by an enzyme digestion solution containing 2.5 M NaCl, 10.0 mM EDTA, 10.0 mM Tris-HCl, and 0.5 mg mL^{-1} proteinase K at pH 7.4 at 37 ºC for 2 h.

Electrophoresis was carried out at 12 V for 30 min in an electrophoresis buffer with sodium acetate and Tris buffer at pH 9.0. The slide was then treated through washing and dehydrating steps with 1.0 M ammonium acetate in ethanol and absolute ethanol, and dried in the dark. Before imagining, the slide was rehydrated in freshly prepared 5% DMSO in 10 mM NaH_2PO_4 solution and was stained with 1.0 μM YOYO-1 in 5% DMSO for 5 min in the dark. The microgels were imaged with a fluorescence microscope (Ex/Em = 491/509 nm) with 100x magnification for DNA tail length analysis. Images were analyzed in ImageJ for tail length measurements. Analysis at each passage was performed with three replicates with 50~150 DNA tails analyzed with each condition. D'Agostino & Pearson normality test was performed on each data set, followed by the non-parametric Kruskal-Wallis test and the Dunn's multiple comparisons test for statistical analysis.

Resister generation frequency

NMC/ion eqv.-exposed and unexposed cultures were set up in triplicate and 20 mL of the cultures at 72 h were used for harvesting the cells by centrifugation at 4000 x *g* for 10 min at room temperature. The bacterial pellet was resuspended in 200 μL of the supernatant. From the resuspended mixture, 20 μL were kept for CFU plating and the remainder (180 μL) was plated on antibiotic-containing plates with 200 μg/ml nalidixic acid, 25 μg/ml rifampicin, and 100 μg/ml erythromycin. Once plated, samples were incubated at 30 ºC for 48-72 h. Colonies observed on the antibiotic-containing plates were considered as the resister mutants. To calculate the resister generation frequency, the number of colonies found on the antibiotic plates was divided by the total number of cells plated (from CFU plating) on that particular plate. Higher values represent higher resister generation frequency or mutation rate(38, 39).

Mutation analysis

Colonies obtained from antibiotic-containing plates were picked and cultured in LB media. Genomic DNA was isolated from liquid inoculated cultures using a DNA purification kit

following the manufacturer's protocol (Promega, Wizard® Genomic DNA Purification Kit, A1120), the final elution was performed in ultra-pure, autoclaved milliQ water. Genomic DNA was used in a polymerase chain reaction (PCR) with specific primers for the mutation hotspot region in the antibiotic resistance-determining region of the genes. For nalidixic acid, the hotspot region named QRDR (quinolone resistance-determining region) in the *gyrA* gene(40-42) was PCR amplified, and the hotspot region RRDR for rifampicin resistance-determining region in the *rpoB*(39, 43, 44) gene was PCR amplified using high fidelity DNA polymerase, Phusion polymerase (New England Biolabs, E0553S). The PCR-amplified product was purified using a PCR purification kit (GeneJET PCR purification kit, Thermo Scientific, K0701) and the sequenced was amplified using the specific primers (Table S1) by Sanger sequencing (ACGT Inc., DNA sequencing services). PCR amplifications and sequencing were performed for the colonies obtained from the resister plates from all samples, as well as the starter culture from the glycerol stock to confirm the sequence of the parent strain or culture used (never exposed or never sub-cultured). Mutations were identified by aligning the sequences using an online multiple sequence alignment tool, Clustal Omega from EMBL-EBI(45) and mismatches were examined.

Results and Discussion

Prolonged exposure to NMC leads to extensive filamentation in *S. oneidensis*

S. oneidensis was cultured in minimal media and exposed to 25 mg/L of NMC for four passages where cells were sub-cultured every 72 h (passage A-D; **Fig. 1a**). This NMC concentration was chosen based on previous work where the response of *S. oneidensis* was assessed at various concentrations of NMC and the first exposure to 25 mg/L NMC resulted in significant lethality, which diminished as the organism started to adapt(12). Cells from all the passages were imaged with a brightfield microscope to measure length. As seen before, the

average cell length remained constant through passages A and B (**Fig. 1b, c, f, g**) and began to increase during the third re-exposure to NMC (**Fig. 1d, h**). In passage D, NMC-exposed cells exceeding 40 μm in length were observed although the population is not homogenous at any point in the experiment (**Fig. 1e, i**). We did not observe any further increase in cell length or a larger proportion of cells with greater lengths in further passages (data not shown). Hence, we focused our studies on passage D.

Exposure to NMC led to ROS increase in *S. oneidensis*

Given that increased cell length or filamentation is often a stress response, we hypothesized that the observed changes in *S. oneidensis* resulted from exposure to exogenous ROS (i.e., from NMC dissolution) and/or organismal generation of ROS. To test this supposition, we treated samples with a cell permeable ROS scavenger, thiourea (TU), at a non-lethal concentration to examine its impact on bacterial filamentation (0.1 mM; **Fig. S1a** and **S1b**). Thiourea indeed decreased the extent of filamentation in NMC-exposed cells and the length of the bacterial cells did not increase significantly compared to the passaged control (**Fig. 1d** and **1e**). Because we had to balance the effects of thiourea on the cells with its utility as a scavenger, we could not examine higher concentrations to determine if this would completely prevent cell elongation. However, the observed decrease in filamentation in the presence of thiourea indicated a role of ROS during NMC exposure.

We also sought to evaluate if the bacterial cells were actively producing ROS using a cell permeable ROS-sensitive dye, 2',7'-dichlorodihydrofluorescein diacetate (H_2DCFDA or DCFDA). Cells from all passages at 72 hr post inoculation were incubated with DCFDA and imaged. NMC-exposed bacteria in all passages exhibited higher fluorescence as compared to unexposed cells in that passage (**Fig. 2a** and **2b**). To investigate ROS levels in the population as compared to individual cells, the fluorescence intensities of DCFDA-stained cells were

measured using flow cytometry, as well as a fluorescent plate reader method. Flow cytometry confirmed the increase in ROS upon NMC exposure in all passages. A shift in the population with higher DCFDA fluorescent signal was observed in NMC-exposed cultures (red population in the P1 gate; **Fig. 2c** and **2d**; **Fig. S2**). Importantly, addition of ROS scavengers like TU to the growing cultures decreased ROS levels in the population, confirming the presence of ROS in the NMC-exposed samples (e.g., shift of red population to left by 10.7% in NMC-exposed populations; compare **Fig. 2d** and **2g**). Again, because we needed to use a sub-lethal concentration of TU, ROS levels were not expected to drop completely (**Fig. S1**). We next investigated ROS production when *S. oneidensis* was exposed to the metal ions equivalent to what is dissolved from NMC during the course of a passage.(12) Ion exposure also resulted in an increase in ROS-specific fluorescence but not as marked as that upon NMC exposure (median fluorescence values 15% higher in NMC-exposed population than ion-exposed samples), indicating an NMC-specific effect (**Fig. 2e**; **Fig. S3**). As before, addition of TU decreased the level of ROS (red population shifts left by 8.2%; **Fig. 2e** and **2h**).

Similar results were obtained using a fluorescence-based plate reader method where NMC-exposed cells showed a higher DCFDA-specific fluorescence intensity per cell (per cell data has been calculated from C.F.U.) as compared to the unexposed cells in all the passages (**Fig. 2i-2l**). Ion-exposed cells also exhibited higher DCFDA-specific fluorescence intensity per cell than unexposed cells, but this fluorescence was lower than the NMC-exposed cells (**Fig. 2i-2l**). Assays were performed with continuously passaged cells (A to D) meaning that experiments were performed across many days making it difficult to quantitatively compare across data sets as some variability is unavoidable. Negative controls such as minimal media blank, minimal media with NMC, or minimal media with ions samples showed negligible fluorescence and were used for background subtraction from their respective test samples.

Exposure to NMC led to increased hydroxyl radicals in *S. oneidensis*

DCFDA is most informative about the overall level of ROS in the cells, including hydroxyl radicals, hydrogen peroxide, and superoxide radicals. Superoxide radicals in the presence of superoxide dismutase are converted to hydrogen peroxide, which ultimately gives rise to hydroxyl radicals in the presence of free ferrous ion, through the Fenton reaction(46). Hydroxyl radicals are extremely reactive due to their high one-electron reduction potential (~+1.8 V)(47). We employed a hydroxyl radical-specific dye, hydroxyphenyl fluorescein (HPF), to probe this reactive species. We found that hydroxyl radical levels were significantly higher in NMC-exposed bacteria as compared to unexposed cultures in all the passages (**Fig. 3a–3d**). Ion-exposed cells also exhibited higher HPF-specific fluorescence intensity per cell than unexposed cells, but this fluorescence was lower than the NMC-exposed cells (**Fig. 3a–3d**). Flow cytometry also confirmed that the hydroxyl radical levels were higher during NMC-exposure, which was observed by a shift of 33% to a more fluorescent population (red colored population shift) as compared to the WT cells (P1 gate, **Fig. 3e** and **3f**; **Fig. S4**). The P1 gate was assigned on the basis of auto-fluorescent samples (unstained) and not the WT controls, thus, the WT sample showed minimal ROS in the cultures, which might be due to the regular respiratory-related process in the cells. The ion-exposed cells exhibited lower hydroxyl radical levels than upon NMC exposure (**Fig. 3g**). The median fluorescence of NMC-exposed samples in the P1 gated population was 32.0% higher than that of the ion-exposed samples in the P1 gate (compare **Fig. 3f** and **3g**), confirming higher hydroxyl radical content in the presence of NMC. Cells cultured in the presence of a hydroxyl scavenger, TU, along with NMC or ions showed a decrease in the hydroxyl radical level compared to growth without the scavenger (**Fig. 3i** and **j**). This decrease was observed by a shift of the red population towards the left by 27.3% in the case of NMC-exposed populations and 2.30% in the case of ion-exposed samples. Complete reduction is not expected due to the use of a sub-lethal concentration of TU (see

above). The ion equivalent control also showed HPF fluorescence, which is higher than the unexposed cultures but lower than NMC-exposed samples, confirming a combinatorial effect of released ions and a nanoparticle-specific effect during NMC exposure (**Fig. 3g**). The observed presence of hydroxyl radicals likely contributes to lethality/toxicity in these cultures as it is one of the most toxic ROS and can lead to cell death and/or DNA mutagenesis(48).

Hydrogen peroxide release during NMC exposure

Given that hydroxyl radicals are formed upon NMC exposure, we sought to determine if this can be correlated to the levels of hydrogen peroxide in the cultures. An Amplex-Red assay was used to quantify the hydrogen peroxide concentration and compare among differing conditions. A standard curve was generated using H_2O_2 solutions, enabling absolute quantification of H_2O_2 in the bacterial cultures (**Fig. S5a**). Amplex Red is cell impermeable and therefore only reports on H_2O_2 that has diffused out of the cells. Cells exposed to NMC showed the highest levels of H_2O_2 as compared to unexposed and ion exposed samples (**Fig. 4a**). Cell cultures from all four passages showed higher H_2O_2 in the NMC-exposed samples as compared to the unexposed cultures (**Fig. 4b** and **S6a–S6c**). A gradual increase in the concentration of H_2O_2 was observed from passages A to D, where passage D exhibited the highest H_2O_2 concentration from NMC-exposed bacteria (**Fig. 4b**), confirming that NMC exposure leads to an increase in H_2O_2 over time. Addition of the H_2O_2 scavenger, dimethyl thiourea (DMTU), in the cell cultures decreased the H_2O_2 concentrations, confirming the presence and detection of H_2O_2. Cultures grown in the presence of metal ions alone also resulted in more H_2O_2 than unexposed cells but less than NMC-exposed cultures, except in passages B and C (**Fig. 4a** and **S6a–S6c**).

With the confirmation of ROS formation in bacterial cultures upon NMC exposure, we sought to determine if it was generated by the nanomaterial, the bacteria, or both. Given that several nanomaterials are known to generate ROS, it is possible that the observed increase in

ROS during passages C and D is solely the result of ROS release from NMC. However, it is also possible that the toxic impact of NMC on *S. oneidensis* triggers ROS generation in the bacteria. To differentiate biotically and abiotically-generated ROS, we again employed the Amplex Red dye assay and assessed H_2O_2 concentrations upon incubation of NMC in the media both with and without cells. The later experiment provides information on the contribution of NMC to the total H_2O_2 concentration in the media. We found that when the H_2O_2 levels are monitored for the initial 60 minutes in all passaged cultures, medium containing NMC alone generates comparable amount of H_2O_2 as observed in passage B of the organism exposure experiments (**Fig. 4c**). These data indicate that the H_2O_2 generated in early passages is largely the result of NMC transformation in aqueous media. It should be noted that the H_2O_2 concentration from NMC remained similar over the course of each 72 hr passage (**Fig. S5b**). At the later timepoints in the exposure experiments, passages C and D, the amount of H_2O_2 increases, which is indicative of bacterial production of ROS (**Fig. 4b** and **4c**). H_2O_2 generation by unexposed bacteria is minimal (**Fig. 4a**).

When bacteria encounter environmental toxins, an SOS response is activated resulting in the generation of high levels of ROS within the cellular milieu(26). We anticipate that NMC exposure activates the SOS response as this material is initially lethal to most cells(12). We postulate that the elevated levels of ROS in later passages is the result of SOS activation as the cells started to adapt (H_2O_2 released in passage C and D highlighted by yellow arrows; NMC-only indicated with brown arrow, **Fig. 4c**). Together, these data confirm that H_2O_2 is produced both by NMC transformation in the media and by prolonged exposure of *S. oneidensis* to this toxic material.

We used the same assay to evaluate abiotic H_2O_2 production from the metal ion solutions, which we found to be low relative to NMC solutions (**Fig. S6d**), which indicates that the vast majority of the H_2O_2 released in cultures exposed to metal ions is contributed by the

bacterial cells. Most of the passage data suggest that the levels of H_2O_2 are higher in NMC-exposed cultures than in ion-exposed ones. The exception to this trend is passage B, in which the amount of H_2O_2 from NMC- and ion-exposed cultures is not significantly different. Indeed, the Amplex red assay confirmed that NMC exposure induces the formation of more H_2O_2 from bacteria as compared to its ion equivalents, indicating a nanomaterial-specific effect.

Overall, we conclude that NMC increased H_2O_2 levels in cell cultures by both the direct release of abiotically-produced H_2O_2 and by inducing stress, causing H_2O_2 generation by the bacteria, perhaps through the SOS response. It is well-known that SOS activation can alter or halt normal bacterial processes, such as cell division, to repair DNA damage(15). Indeed, effects on cell division can ultimately lead to cellular filamentation, which we have observed both in this study and in earlier work(12, 49) (**Fig. 1e** and **1i**).

Presence of ROS-containing vesicles during NMC exposure

To investigate the spatial distribution of ROS in stressed bacteria, we treated NMC-exposed cells with DCFDA followed by microscopy visualization, from all the four passages. Most cells in passage D showed increased fluorescence signal compared to NMC unexposed ones with no fluorescence signals (calculated as fluorescence per unit length, also compare **Fig. 2a-2b**), with a small population of highly elongated cells (>25 μm) exhibiting lower or no fluorescence (**Fig. S7a**). These data are indicative of heterogeneity in the ROS levels within the cells, which correlates with the spread in the DCFDA/HPF-stained population observed with flow cytometry (**Fig. 2d**). We also observed that a proportion of the cells contained vesicles ranging from 0.1-1 μm in diameter. These vesicles contained DCFDA fluorescence indicating that they harbor ROS (**Fig. 5a–5d**; **Fig. S7b–S7m**). Staining of the cells with Hoechst dye showed the presence of DNA in cells of all sizes but absence of DNA in ~70% of the vesicles (**Fig. 5e** and **g**; **Fig. S8**). To determine if the vesicles are membrane bound, we

stained them with FM4-64 and confirmed the presence of lipid membrane at the periphery of the vesicles (**Fig. 5h**).

To further evaluate the make-up of the vesicle architecture, we next investigated whether they are encompassed by the crucial cell wall structure, peptidoglycan. Peptidoglycan can be labelled using fluorescent D-amino acids (FDAAs), which become incorporated into the stem peptide of the peptidoglycan chains(50, 51). Using the orange-red TAMRA-based FDAA, RADA, to label the peptidoglycan layer, we found that the vesicles exhibited fluorescence confirming the presence of peptidoglycan (**Fig. 5f** and **S8**). Formation of vesicles that contain both peptidoglycan and lipid membrane often results from pinching off of a portion of the cells, typically at the division site or towards the poles(52). As these vesicles contained ROS, we hypothesize that the adapted cells may be using them to remove excess ROS, which would otherwise be highly toxic. Consistent with this hypothesis, we also found that some vesicles eventually burst while still attached to the cells, which was visualized with live-cell time-lapsed imaging (**Fig. 6a–6o**). Once a vesicle bursts, the intensity of the DCFDA stain of this cell drops dramatically, which is not observed in cells with no vesicles (**Fig. 6a–6g**).

DNA damage in NMC-exposed bacterial cells

Previous work has indicated that abiotic ROS generated from another transition metal oxide, lithium cobalt oxide, can induce bacterial DNA damage in *B. subtilis*(14). As such, we examined the extent of DNA damage from multiple passages of NMC-exposed *S. oneidensis* using the comet assay to assess double-strand DNA breakage. The distribution of DNA tail lengths of single cells from bacterial culture in different passages upon exposure to NMC compared to those from control (WT) is illustrated as a violin plot (**Fig. 7a-d**). In all four passages, NMC exposure induced significantly longer bacterial DNA tails than those from the control conditions, suggesting more severe DNA damage upon NMC exposure across all

passages. The addition of thiourea (TU) to NMC-containing cultures reduced the extent of DNA damage, indicated by the shorter overall DNA tail lengths. The difference is most stark in passage D (**Fig. 7d**). The impact of TU as an ROS quencher on mitigating bacterial DNA damage (**Fig. 7** and **S9**) echoes the results obtained in the evaluation of bacterial filamentation (**Fig. 1**) and in reducing intracellular ROS signals in flow cytometry (**Fig. 2** and **3**). Therefore, NMC exposure across multiple passages induced increased intracellular ROS, as measured from the levels of H_2O_2 and hydroxyl radicals. Since DNA is a well-known biomolecular target of hydroxyl radicals(53), DNA damage in all passages is observed, and the damage can be mitigated in the presence of a ROS scavenger.

ROS leading to DNA mutation

As NMC exhibited DNA damaging effects in the bacterial cells due to the production of ROS, we sought to determine if this ROS also promoted random point mutations in the genome. Rather than performing whole genome sequencing, we opted for a more straightforward selection-based strategy. NMC-exposed and unexposed cells were plated on high (lethal) concentrations of antibiotics as a selection criterion and the resister generation frequency was calculated (**Fig. 8a** and **b**). While NMC exposure could cause fitness-conferring mutations that are specific to this material within the genome, ROS-mediated mutations are random and would thus result in potentially advantageous changes in antibiotic-resistance-determining regions of the genome. As a result, cells with mutations that aid in growth of the bacteria under higher antibiotic concentrations can easily be identified and characterized by sequencing the specific region of the genome associated with antibiotic resistance. For this purpose, we used three antibiotics that function through different mechanisms of action: nalidixic acid (DNA gyrase inhibition), rifampicin (RNA polymerase inhibition) and erythromycin (protein synthesis inhibition). We found that a larger number of colonies were

able to survive at higher concentrations of all three antibiotics following NMC exposure as compared to the unexposed cultures (**Fig. 8c; S10a** and **b**). These data likely indicate a higher rate of random mutation among NMC-treated cells.

To determine the specific mutations within these strains, single colonies from the antibiotic-containing plate were selected, cultured in liquid media without antibiotics, the genomic DNA isolated, and the resistance-determining region for nalidixic acid was PCR amplified using high fidelity DNA polymerase. The PCR amplicons were sequenced using specific primers and the sequences compared. Colonies that were grown on nalidixic acid-containing plates showed the presence of point mutations (**Fig. 8d** and **Table S1** and **2**), which have been reported in other bacterial species in a clinical setting that gained resistance against nalidixic acid(40-42). These 'C' to 'T' point mutations also translated to an amino acid change from serine to leucine for most of the colonies. These mutations are usually random in nature as the causative agent is ROS. Thus, some colonies exhibited different a point mutation of 'C' to 'G' resulting in change from serine to tryptophan. These amino acid alterations would affect the protein functionality, ultimately making the mutated bacterial cells resistant to the antibiotic. Unpassaged cells (WT-stock) did not have these mutations (**Fig. 8d**), confirming that more mutations either developed during NMC treatment or on the antibiotic-containing plate. Clearly, the presence of NMC increases the potential of cells to inflict genomic mutations, which could be due to the higher levels of hydroxyl radicals (**Fig. 3e** and **f**). Higher resister generation frequency in NMC-exposed cells was also seen when cells were plated on rifampicin and erythromycin (**Fig. S10**).

These results are consistent with our DNA damage assay and indicate that *S. oneidensis* undergoes more rapid mutation, and thus has a higher mutation frequency upon NMC exposure, perhaps due to greater ROS concentrations. This increase in mutation frequency also implies that there may be random genome-wide mutations that could affect processes such as

metabolism, as is indicated by our previously-reported data showing changes in the respiratory abilities of bacteria upon NMC exposure(10).

Conclusion

Nanomaterial-induced toxicity and resistance have largely been studied in the context of antibacterial agents for medicinal purposes. Relatively little is known about how prolonged exposure to engineered nanomaterials that are made for other purposes affects microbes. However, acute exposure to many metal nanomaterials is toxic to various organisms, including bacteria. From our studies, it is evident that NMC is toxic to a ubiquitously present and environmentally relevant bacterial species, *S. oneidensis*. Initial exposure causes widespread cell death while prolonged contact results in bacterial filamentation, ROS generation likely due to triggering of the SOS response, and DNA damage. We hypothesize that higher intracellular ROS levels led to this DNA damage and may also cause transformation of other biomolecules.

The exact mechanism of ROS production by NMC is not yet fully understood. However, the similar nanomaterial, LCO, also produces H_2O_2 upon dissolution that damages bacterial cells(14). It has been reported that NMC does not need to come into physical contact with the bacteria to cause damage and that Ni and Co ions released during dissolution(13), along with abiotically-produced ROS, can enter bacterial cells and trigger intracellular ROS responses. Our data further support this model.

Our data also show that chronic exposure to NMC resulted in higher rates of DNA mutation. Indeed, we are the first to report a higher frequency of antibiotic resistance evolution in bacteria following nanoparticle exposure. There are reports of the emergence of antibiotic resistance in filamented(54-56) or multinucleated *E. coli* upon antibiotic treatment,(57) the former phenotype being seen in our studies. During filamentation, random mutations can be

generated, and only those bacteria that gain a beneficial mutation can survive and become resistant towards specific antibiotics or stressors.

Our results indicate that *S. oneidensis* exposure to NMC is initially lethal to most of the bacterial population. However, extended exposure leads to adaptation and cell populations with phenotypic variations, likely due at least in part to an increased rate of random mutation. We also found that bacteria under NMC stress can generate membrane-bound vesicles, perhaps as a mechanism to expel ROS(58). These vesicles may also be released into the surroundings and act as signals to alert cells in the vicinity of toxic stress exposure. Overall, this study indicates the changes that bacteria undergo during nanomaterial exposure, variations in phenotype and acquisition of non-specific mutations, underscoring the importance of evaluating the environmental impact of technologically relevant engineered nanomaterials such as NMC.

Conflicts of Interest

The authors declare no competing interest.

Acknowledgements

This material is based upon work supported by the National Science Foundation under Grant No. CHE-2001611, the NSF Center for Sustainable Nanotechnology (CSN). The authors gratefully acknowledge use of shared University Flow Cytometry Resource at the University of Minnesota-Twin cities. We thank S. L. Mitchell for helpful discussions and suggestions. The authors gratefully acknowledge use of facilities and instrumentation at the UW-Madison Wisconsin Centers for Nanoscale Technology (wcnt.wisc.edu) partially supported by the NSF through the University of Wisconsin Materials Research Science and Engineering Center (DMR-1720415).

Figure Legends

Figure 1. Exposure of *S. oneidensis* to NMC nanomaterials and effect on bacterial cell length. (a) Experimental layout of NMC exposure through multiple passages from A to D; (b–e) Length of bacteria in all four passages during different culture conditions including unexposed wild-type cells (WT), wild-type cells with ROS scavenger thiourea, 0.1 mM (WT+TU), NMC-exposed cells (WT+NMC) and cells exposed to NMC and ROS scavenger thiourea (WT+NMC+TU); (f) Representative images of unexposed WT cells at passage A; (g) cells exposed to NMC during passage A; (h) NMC-exposed cells at passage C and (i) NMC-exposed cells at passage D. Significance calculated from three independent experiments using unpaired t-test, where *, *** indicate $p \leq 0.05$ and $p \leq 0.001$, respectively.

Figure 2. Determination of reactive oxygen species (ROS) formation upon NMC or ion eqv. exposure of bacterial cells using DCFDA dye. (a) Representative microscopic images of NMC-unexposed and (b) NMC-exposed cells after DCFDA dye treatment. (c–h) Flow cytometry of unexposed, NMC or ion eqv.-exposed cells stained with DCFDA, the percentage written in the P1 gate represents the percentage of the population present in P1 gate with higher DCFDA-based fluorescence signal than the whole population, (f–h) in the presence of ROS scavenger thiourea, 0.1 mM (TU). (i–l) DCFDA-based fluorescence intensity of cells unexposed, exposed to NMC, and exposed to ions from passage A to D. The fluorescence intensities have been normalized to CFU to obtain fluorescence intensity per cell. Significance calculated from three independent experiments using unpaired t-test, where *, **indicate $p \leq 0.05$ and $p \leq 0.01$, respectively.

Figure 3. Determination of hydroxyl radical presence upon NMC or ion eqv. exposure of bacterial cells using HPF dye. (a–d) HPF-based fluorescence intensity of cells unexposed, exposed to NMC, and exposed to ions from passage A to D. The fluorescence intensity values have been normalized to CFU to obtain fluorescence intensity per cell. Significance calculated from three independent experiments using unpaired t-test, where *, **, *** indicate $p \leq 0.05$, $p \leq 0.01$ and $p \leq 0.001$ respectively. (e–j) Flow cytometry of unexposed, NMC or ion eqv.-exposed cells stained with HPF dye, the percentage written in the P1 gate represents the percentage of the population present in P1 gate with higher HPF-based fluorescence signal than the whole population, (h–j) in the presence of ROS scavenger thiourea, 0.1 mM (TU).

Figure 4. Estimation of hydrogen peroxide concentrations in the cultures exposed to NMC or ion eqv. using Amplex Red assay. (a) Concentration of H_2O_2 in the unexposed/NMC-exposed/ion eqv.-exposed cultures and in the presence of H_2O_2 scavenger dimethyl thiourea (DMTU) from passage D. The data has been plotted from three independent experiments and significance calculated using unpaired t-test where *, **indicate $p \leq 0.05$ and $p \leq 0.01$, respectively. (b) Concentration of H_2O_2 of NMC-exposed cultures at different passages, as well as only NMC in minimal media. (c) Time course of concentration of H_2O_2 of NMC-exposed cultures at different passages, as well as only NMC in minimal media with 15 min interval for 60 min.

Figure 5. Microscopic images of NMC-exposed cells from passage D. (a) and (c) Brightfield images of cells with visible vesicles, (b) and (d) stained with DCFDA for ROS, (e) and (g) stained with Hoechst for DNA staining, (f) stained with TAMRA-based fluorescent D-amino acid RADA for peptidoglycan staining, and (h) stained with FM 4-64 for lipid membrane staining. Scale bar is 20 μm.

Figure 6. Microscopic images of NMC-exposed cells from passage D. (a), (b) and (f) Brightfield images of cells with visible vesicles, (c) and (g) stained with DCFDA, (d) stained with RADA, (e) stained with Hoechst. (h–o) Live cell time-lapse imaging of NMC-exposed cells from passage D, (h–k) set 1 and (l–o) set 2. Scale bar is 20 μm.

Figure 7. Comet assay bacterial tail length analysis in violin plot shows DNA double strand breakage in NMC-exposed *S. oneidensis* after passages A (a), B (b), C (c), and D (d) upon exposure to NMC or NMC with thiourea (TU). Asterisks denote statistically significant differences using the Kruskal-Wallis test followed by Dunn's multiple comparisons test, where ** indicate $p \leq 0.01$ and **** for $p \leq 0.0005$. The dash line in the violin plot denotes the average, and the dotted lines represent the quartiles.

Figure 8. Resister and mutation analysis. (a) Experimental layout of unexposed/NMC/ion-exposed cells from passage D plated on antibiotic-containing and antibiotic-free LB agar plates, (b) Calculation of resister generation frequency from the bacterial colony counts, (c) Resister generation frequency of passage D cells with 20 mg/L nalidixic acid, (d) Sequencing results for PCR-amplified QRDR (quinolone resistance-determining region) of *gyrA* gene from different colonies (WT passaged, two NMC exposed and two ion exposed from duplicate experiments) picked from nalidixic acid plates compared to unexposed, un-passaged bacterial stock or starter culture. Point mutation at 248 nucleotide position in the *gyrA* gene has been highlighted in cyan and green while the WT nucleotide is in yellow, un-mutated in stock. Stars at the bottom denote sequence similarity at each nucleotide position and the gap denotes mutation.

References

1. Johnson CS, Li N, Lefief C, Vaughey JT, Thackeray MM. Synthesis, characterization and electrochemistry of lithium battery electrodes: x Li2MnO3·(1− x) LiMn0. 333Ni0. 333Co0. 333O2 (0≤ x≤ 0.7). Chemistry of Materials. 2008;20(19):6095-106.
2. Belharouak I, Sun Y-K, Liu J, Amine K. Li (Ni1/3Co1/3Mn1/3) O2 as a suitable cathode for high power applications. Journal of Power Sources. 2003;123(2):247-52.
3. Li J, Klöpsch R, Stan M, Nowak S, Kunze M, Winter M, et al. Synthesis and electrochemical performance of the high voltage cathode material Li [Li0. 2Mn0. 56Ni0. 16Co0. 08] O2 with improved rate capability. Journal of Power Sources. 2011;196(10):4821-5.
4. Whittingham MS. Lithium batteries and cathode materials. Chemical reviews. 2004;104(10):4271-302.
5. Song HK, Lee KT, Kim MG, Nazar LF, Cho J. Recent progress in nanostructured cathode materials for lithium secondary batteries. Advanced Functional Materials. 2010;20(22):3818-34.
6. Mukhopadhyay A, Sheldon BW. Deformation and stress in electrode materials for Li-ion batteries. Progress in Materials Science. 2014;63:58-116.
7. Hamers RJ. Energy storage materials as emerging nano-contaminants. Chemical research in toxicology. 2020;33(5):1074-81.
8. Maurer-Jones MA, Gunsolus IL, Murphy CJ, Haynes CL. Toxicity of engineered nanoparticles in the environment. Analytical chemistry. 2013;85(6):3036-49.
9. Feng ZV, Miller BR, Linn TG, Pho T, Hoang KNL, Hang MN, et al. Biological impact of nanoscale lithium intercalating complex metal oxides to model bacterium B. subtilis. Environmental Science: Nano. 2019;6(1):305-14.
10. Hang MN, Gunsolus IL, Wayland H, Melby ES, Mensch AC, Hurley KR, et al. Impact of nanoscale lithium nickel manganese cobalt oxide (NMC) on the bacterium Shewanella oneidensis MR-1. Chemistry of Materials. 2016;28(4):1092-100.
11. Niemuth NJ, Curtis BJ, Laudadio ED, Sostare E, Bennett EA, Neureuther NJ, et al. Energy Starvation in Daphnia magna from Exposure to a Lithium Cobalt Oxide Nanomaterial. Chemical Research in Toxicology. 2021;34(11):2287-97.
12. Mitchell SL, Hudson-Smith NV, Cahill MS, Reynolds BN, Frand SD, Green CM, et al. Chronic exposure to complex metal oxide nanoparticles elicits rapid resistance in Shewanella oneidensis MR-1. Chemical science. 2019;10(42):9768-81.
13. Qiu TA, Guidolin V, Hoang KNL, Pho T, Villalta PW, He J, et al. Nanoscale battery cathode materials induce DNA damage in bacteria. Chemical science. 2020;11(41):11244-58.
14. Gari MK, Lemke P, Lu KH, Laudadio ED, Henke AH, Green CM, et al. Dynamic aqueous transformations of lithium cobalt oxide nanoparticle induce distinct oxidative stress responses of B. subtilis. Environmental Science: Nano. 2021;8(6):1614-27.
15. Burby PE, Simmons LA. Regulation of cell division in bacteria by monitoring genome integrity and DNA replication status. Journal of Bacteriology. 2020;202(2):e00408-19.
16. Heinrich K, Leslie DJ, Morlock M, Bertilsson S, Jonas K. Molecular basis and ecological relevance of Caulobacter cell filamentation in freshwater habitats. MBio. 2019;10(4):e01557-19.
17. Seeger M, Jerez CA. Phosphate-starvation induced changes in Thiobacillus ferrooxidans. FEMS microbiology letters. 1993;108(1):35-41.
18. Wainwright M, Canham L, Al-Wajeeh K, Reeves C. Morphological changes (including filamentation) in Escherichia coli grown under starvation conditions on silicon wafers and other surfaces. Letters in applied microbiology. 1999;29(4):224-7.

19. Chatterjee S, Raychaudhuri C. Filamentation of Vibrio cholerae cells by furazolidone. Indian journal of experimental biology. 1971;9(2):270-1.
20. Hunt DE, Pittillo RF. Actinobolin-induced filamentation in Escherichia coli. Journal of Bacteriology. 1968;95(2):712-3.
21. Bereksi N, Gavini F, Bénézech T, Faille C. Growth, morphology and surface properties of Listeria monocytogenes Scott A and LO28 under saline and acid environments. Journal of Applied Microbiology. 2002;92(3):556-65.
22. Gill C, Badoni M, Jones T. Behaviours of log phase cultures of eight strains of Escherichia coli incubated at temperatures of 2, 6, 8 and 10° C. International journal of food microbiology. 2007;119(3):200-6.
23. De Jong A, Rombouts F, Beumer R. Behavior of Clostridium perfringens at low temperatures. International Journal of Food Microbiology. 2004;97(1):71-80.
24. Mukherjee A, Cao C, Lutkenhaus J. Inhibition of FtsZ polymerization by SulA, an inhibitor of septation in Escherichia coli. Proceedings of the National Academy of Sciences. 1998;95(6):2885-90.
25. Schoemaker J, Gayda R, Markovitz A. Regulation of cell division in Escherichia coli: SOS induction and cellular location of the sulA protein, a key to lon-associated filamentation and death. Journal of bacteriology. 1984;158(2):551-61.
26. Zhao X, Drlica K. Reactive oxygen species and the bacterial response to lethal stress. Current opinion in microbiology. 2014;21:1-6.
27. Nel A, Xia T, Madler L, Li N. Toxic potential of materials at the nanolevel. science. 2006;311(5761):622-7.
28. Bennett JW, Jones D, Huang X, Hamers RJ, Mason SE. Dissolution of complex metal oxides from first-principles and thermodynamics: Cation removal from the (001) surface of Li (Ni1/3Mn1/3Co1/3) O2. Environmental science & technology. 2018;52(10):5792-802.
29. Fu PP, Xia Q, Hwang H-M, Ray PC, Yu H. Mechanisms of nanotoxicity: generation of reactive oxygen species. Journal of food and drug analysis. 2014;22(1):64-75.
30. Yu Z, Li Q, Wang J, Yu Y, Wang Y, Zhou Q, et al. Reactive oxygen species-related nanoparticle toxicity in the biomedical field. Nanoscale research letters. 2020;15(1):1-14.
31. Xia T, Kovochich M, Liong M, Madler L, Gilbert B, Shi H, et al. Comparison of the mechanism of toxicity of zinc oxide and cerium oxide nanoparticles based on dissolution and oxidative stress properties. ACS nano. 2008;2(10):2121-34.
32. Yin J-J, Liu J, Ehrenshaft M, Roberts JE, Fu PP, Mason RP, et al. Phototoxicity of nano titanium dioxides in HaCaT keratinocytes—generation of reactive oxygen species and cell damage. Toxicology and applied pharmacology. 2012;263(1):81-8.
33. Applerot G, Lipovsky A, Dror R, Perkas N, Nitzan Y, Lubart R, et al. Enhanced antibacterial activity of nanocrystalline ZnO due to increased ROS-mediated cell injury. Advanced Functional Materials. 2009;19(6):842-52.
34. Manke A, Wang L, Rojanasakul Y. Mechanisms of nanoparticle-induced oxidative stress and toxicity. BioMed research international. 2013;2013.
35. Niemuth NJ, Zhang Y, Mohaimani AA, Schmoldt A, Laudadio ED, Hamers RJ, et al. Protein Fe–S Centers as a Molecular Target of Toxicity of a Complex Transition Metal Oxide Nanomaterial with Downstream Impacts on Metabolism and Growth. Environmental Science & Technology. 2020;54(23):15257-66.
36. Mei N, Zhang Y, Chen Y, Guo X, Ding W, Ali SF, et al. Silver nanoparticle-induced mutations and oxidative stress in mouse lymphoma cells. Environmental and molecular mutagenesis. 2012;53(6):409-19.
37. Qiu TA, Gallagher MJ, Hudson-Smith NV, Wu J, Krause MO, Fortner JD, et al. Research highlights: unveiling the mechanisms underlying nanoparticle-induced ROS generation and oxidative stress. Environmental Science: Nano. 2016;3(5):940-5.

38. Pribis JP, García-Villada L, Zhai Y, Lewin-Epstein O, Wang AZ, Liu J, et al. Gamblers: an antibiotic-induced evolvable cell subpopulation differentiated by reactive-oxygen-induced general stress response. Molecular cell. 2019;74(4):785-800. e7.
39. Nair RR, Sharan D, Ajitkumar P. A minor subpopulation of mycobacteria inherently produces high levels of reactive oxygen species that generate antibiotic resisters at high frequency from itself and enhance resister generation from its major kin subpopulation. Frontiers in microbiology. 2019:1842.
40. Reche MP, García de los Ríos JE, Jiménez PA, Rojas AM, Rotger R. gyrA mutations associated with nalidixic acid-resistant salmonellae from wild birds. Antimicrobial agents and chemotherapy. 2002;46(9):3108-9.
41. Sáenz Y, Zarazaga M, Briñas L, Ruiz-Larrea F, Torres C. Mutations in gyrA and parC genes in nalidixic acid-resistant Escherichia coli strains from food products, humans and animals. Journal of Antimicrobial Chemotherapy. 2003;51(4):1001-5.
42. Sánchez-Romero MA, Casadesús J. Contribution of phenotypic heterogeneity to adaptive antibiotic resistance. Proceedings of the National Academy of Sciences. 2014;111(1):355-60.
43. André E, Goeminne L, Cabibbe A, Beckert P, Mukadi BK, Mathys V, et al. Consensus numbering system for the rifampicin resistance-associated rpoB gene mutations in pathogenic mycobacteria. Clinical Microbiology and Infection. 2017;23(3):167-72.
44. Goldstein BP. Resistance to rifampicin: a review. The Journal of antibiotics. 2014;67(9):625-30.
45. Sievers F, Wilm A, Dineen D, Gibson TJ, Karplus K, Li W, et al. Fast, scalable generation of high-quality protein multiple sequence alignments using Clustal Omega. Molecular systems biology. 2011;7(1):539.
46. Winterbourn CC. Toxicity of iron and hydrogen peroxide: the Fenton reaction. Toxicology letters. 1995;82:969-74.
47. Wardman P. Reduction potentials of one-electron couples involving free radicals in aqueous solution. Journal of Physical and Chemical Reference Data. 1989;18(4):1637-755.
48. Kohanski MA, Dwyer, D. J., Hayete, B., Lawrence, C. A., & Collins, J. J. A Common Mechanism of Cellular Death Induced by Bactericidal Antibiotics. Cell. 2007;130(5):797-810.
49. Maslowska KH, Makiela-Dzbenska, K., & Fijalkowska, I. J. The SOS system: a complex and tightly regulated response to DNA damage. Environmental and molecular mutagenesis. 2019;60(4):368-84.
50. Hsu YP, Rittichier, J., Kuru, E., Yablonowski, J., Pasciak, E., Tekkam, S., Hall, E., Murphy, B., Lee, T.K., Garner, E.C. and Huang, K.C. Full color palette of fluorescent d-amino acids for in situ labeling of bacterial cell walls. Chemical science. 2017;8(9):6313-21.
51. Kuru E, Tekkam, S., Hall, E., Brun, Y. V., & Van Nieuwenhze, M. S. Synthesis of fluorescent D-amino acids and their use for probing peptidoglycan synthesis and bacterial growth in situ. Nature protocols. 2015;10(1):33-52.
52. Avila-Calderón ED, Ruiz-Palma, M.D.S., Aguilera-Arreola, M.G., Velázquez-Guadarrama, N., Ruiz, E.A., Gomez-Lunar, Z., Witonsky, S. and Contreras-Rodríguez, A. Outer membrane vesicles of gram-negative bacteria: an outlook on biogenesis. Frontiers in Microbiology. 2021;12:557902.
53. Imlay JA. Pathways of oxidative damge. . Annual review of microbiology. 2003;57:395-418.
54. Justice SS, Hunstad DA, Cegelski L, Hultgren SJ. Morphological plasticity as a bacterial survival strategy. Nature Reviews Microbiology. 2008;6(2):162-8.
55. Yang DC, Blair KM, Salama NR. Staying in shape: the impact of cell shape on bacterial survival in diverse environments. Microbiology and Molecular Biology Reviews. 2016;80(1):187-203.

56. Jones TH, Vail KM, McMullen LM. Filament formation by foodborne bacteria under sublethal stress. International journal of food microbiology. 2013;165(2):97-110.
57. Bos J, Zhang Q, Vyawahare S, Rogers E, Rosenberg SM, Austin RH. Emergence of antibiotic resistance from multinucleated bacterial filaments. Proceedings of the National Academy of Sciences. 2015;112(1):178-83.
58. Schwechheimer C, & Kuehn, M. J. Outer-membrane vesicles from Gram-negative bacteria: biogenesis and functions. Nature reviews microbiology. 2015;13(10):605-19.
59. Mrozik W, Rajaeifar, MA, Heidrich, O, Christensen, P. Environmental impacts, pollution, sources and pathways of spent lithium-ion batteries. Energy Environmental Science, 2021, 14, 6099-6121.

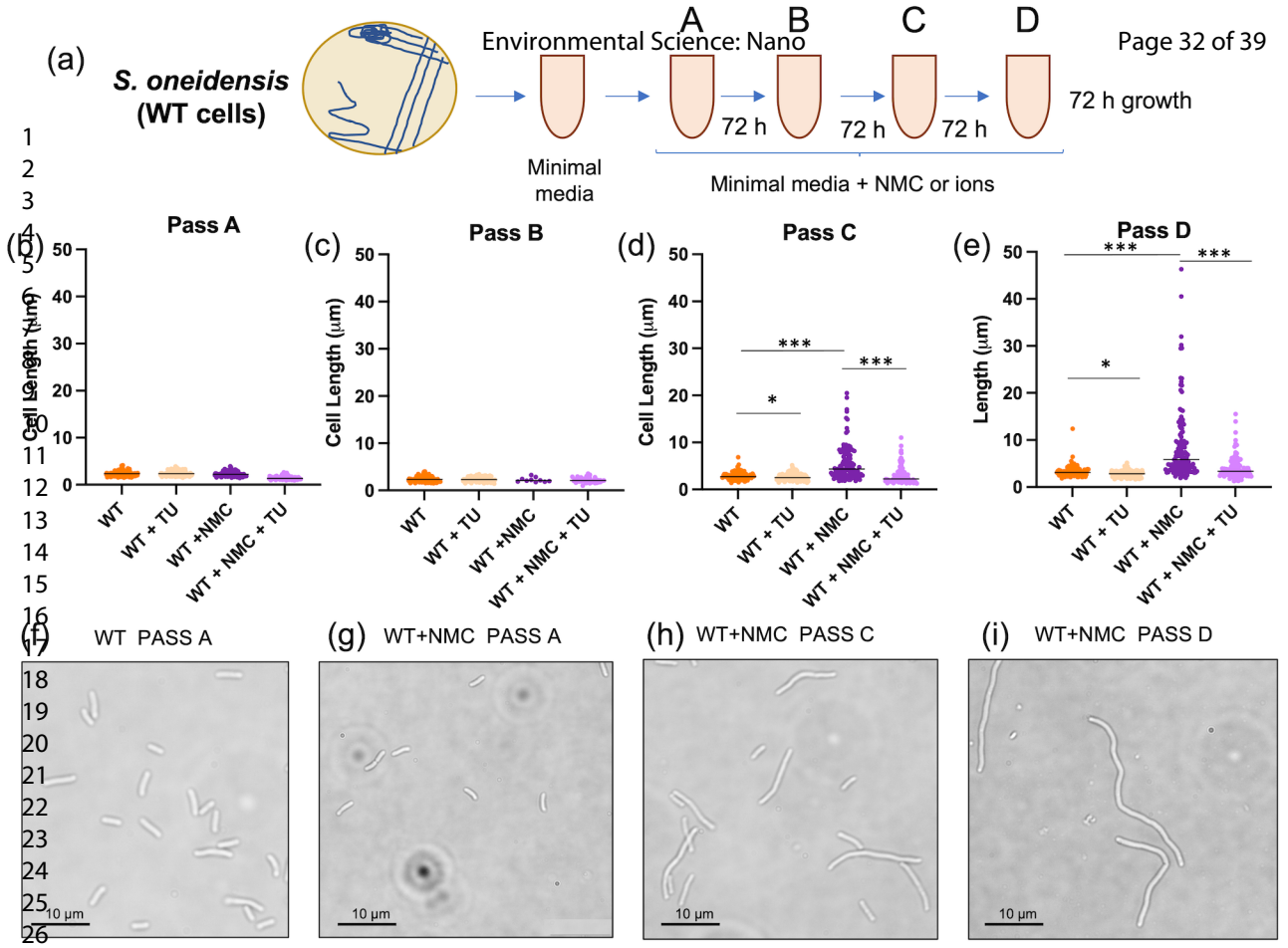
(a)
S. oneidensis
(WT cells)
A
B
C
D
72 h
72 h
72 h
72 h growth
Minimal media
Minimal media + NMC or ions
(b)
Pass A
(c)
Pass B
(d)
Pass C
(e)
Pass D
Cell Length (μm)
Length (μm)
WT
WT + TU
WT +NMC
WT + NMC + TU
*
***
(f)
WT PASS A
(g)
WT+NMC PASS A
(h)
WT+NMC PASS C
(i)
WT+NMC PASS D
10 μm

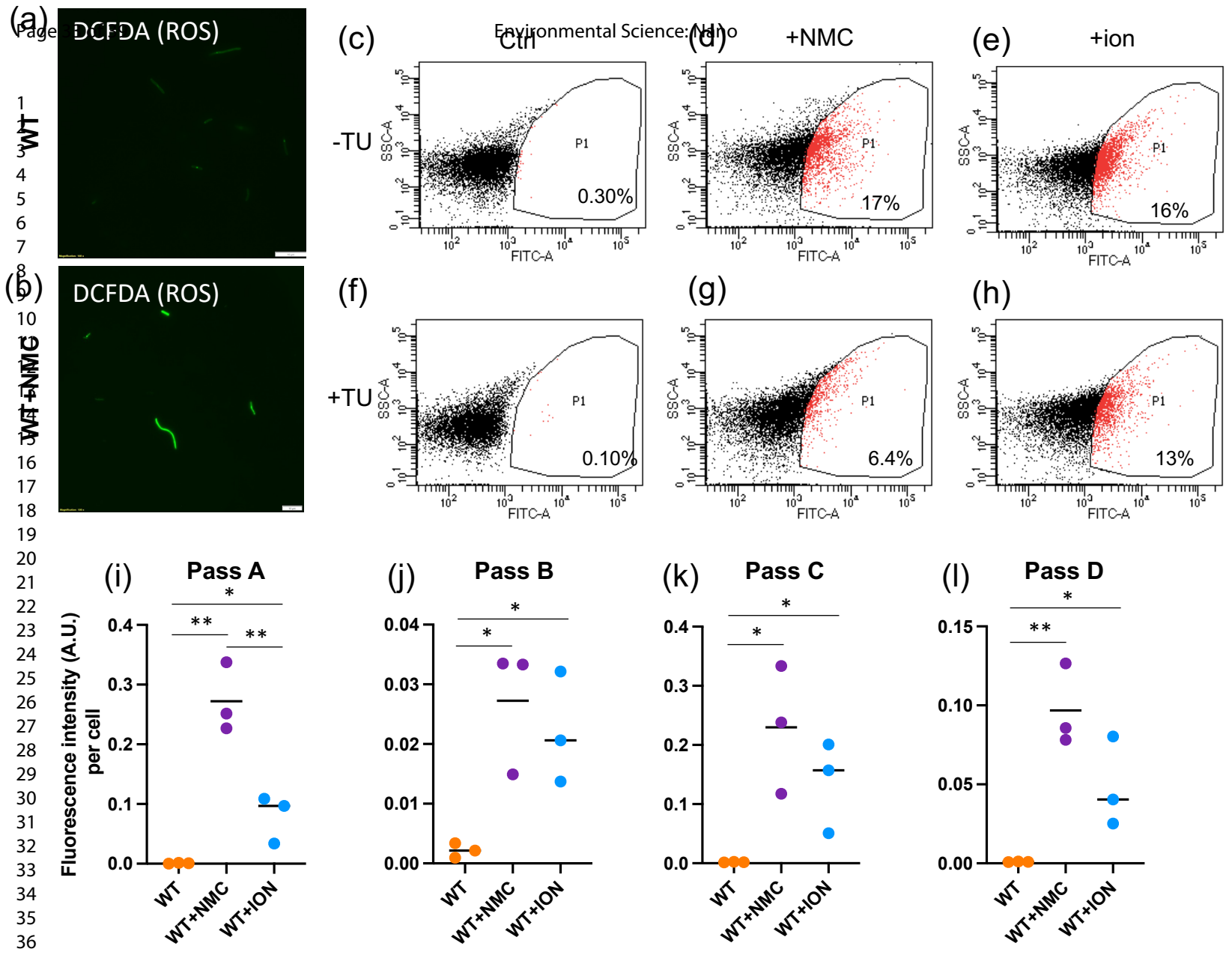
(a)
DCFDA (ROS)
WT
(b)
DCFDA (ROS)
WT+NMC
(c)
Ctrl
-TU
SSC-A
FITC-A
P1
0.30%
(d)
+NMC
17%
(e)
+ion
16%
(f)
+TU
0.10%
(g)
6.4%
(h)
13%
(i)
Pass A
Fluorescence intensity (A.U.) per cell
WT
WT+NMC
WT+ION
(j)
Pass B
(k)
Pass C
(l)
Pass D

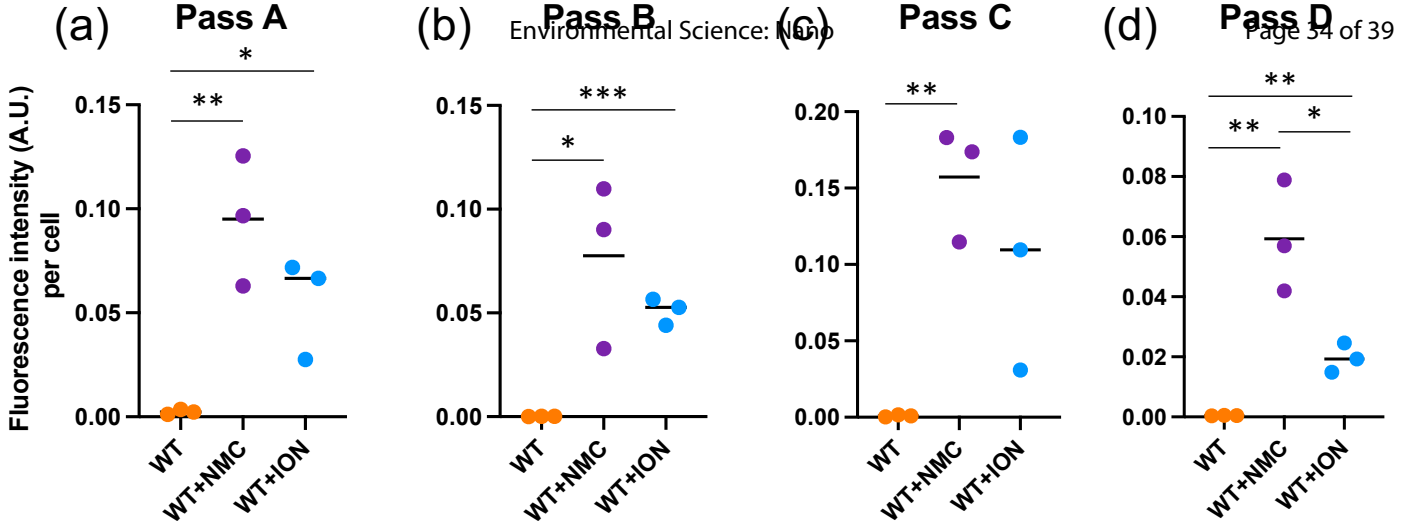
(a) Pass A
(b) Pass B
(c) Pass C
(d) Pass D
Fluorescence intensity (A.U.) per cell
WT
WT+NMC
WT+ION
*
**
***

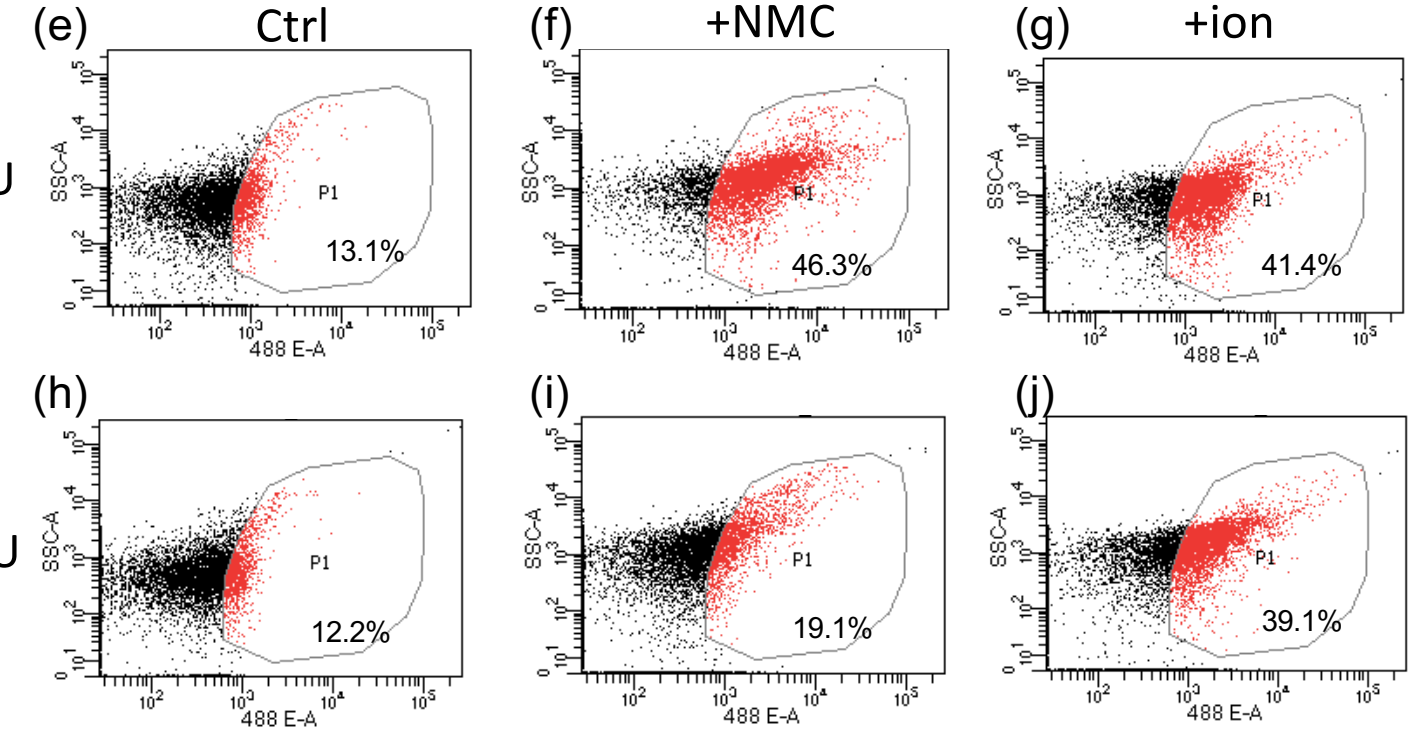
(e) Ctrl
(f) +NMC
(g) +ion
-TU
+TU
SSC-A
488 E-A
P1
13.1%
46.3%
41.4%
12.2%
19.1%
39.1%

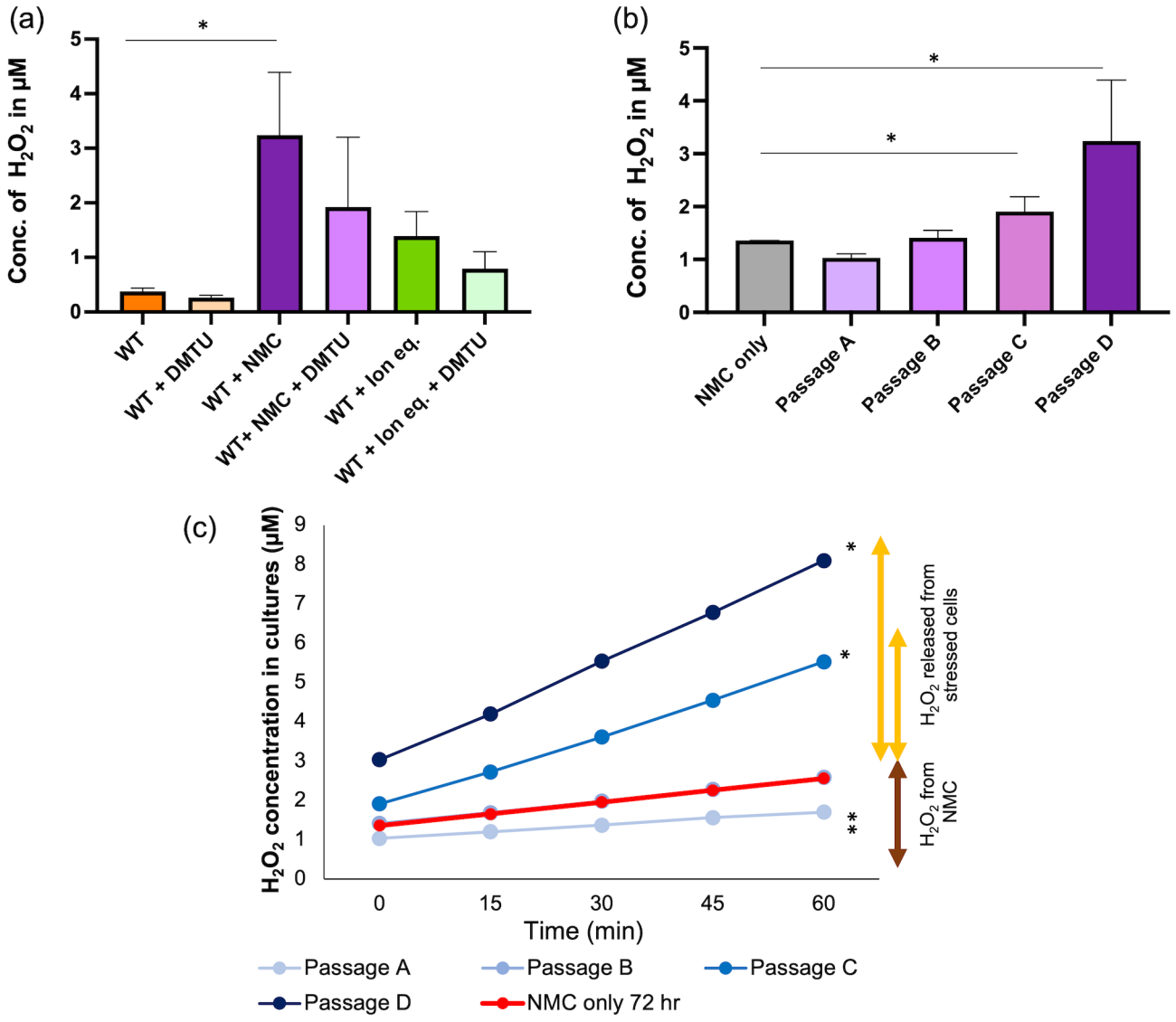
(a)
Conc. of H_2O_2 in µM
WT
WT + DMTU
WT + NMC
WT+ NMC + DMTU
WT + Ion eq.
WT + Ion eq. + DMTU
(b)
Conc. of H_2O_2 in µM
NMC only
Passage A
Passage B
Passage C
Passage D
(c)
H_2O_2 concentration in cultures (µM)
Time (min)
H_2O_2 released from stressed cells
H_2O_2 from NMC
Passage A
Passage B
Passage C
Passage D
NMC only 72 hr

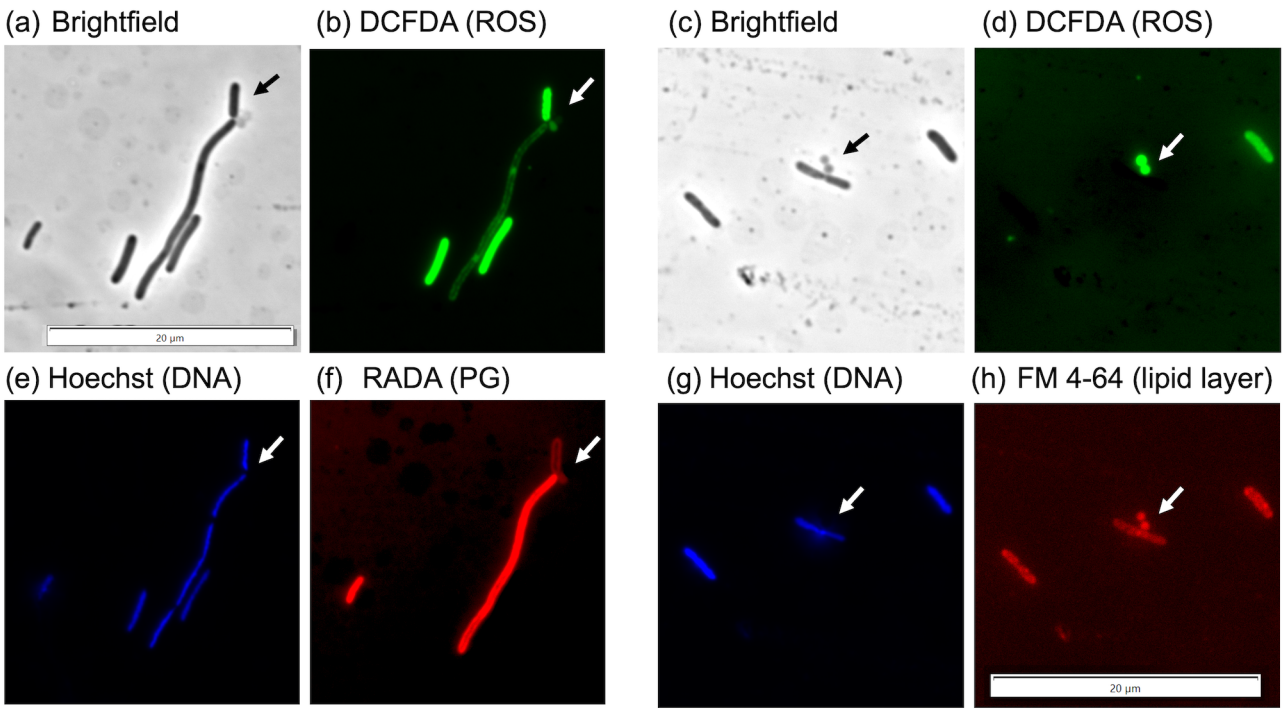
(a) Brightfield
(b) DCFDA (ROS)
(c) Brightfield
(d) DCFDA (ROS)
20 µm
(e) Hoechst (DNA)
(f) RADA (PG)
(g) Hoechst (DNA)
(h) FM 4-64 (lipid layer)
20 µm

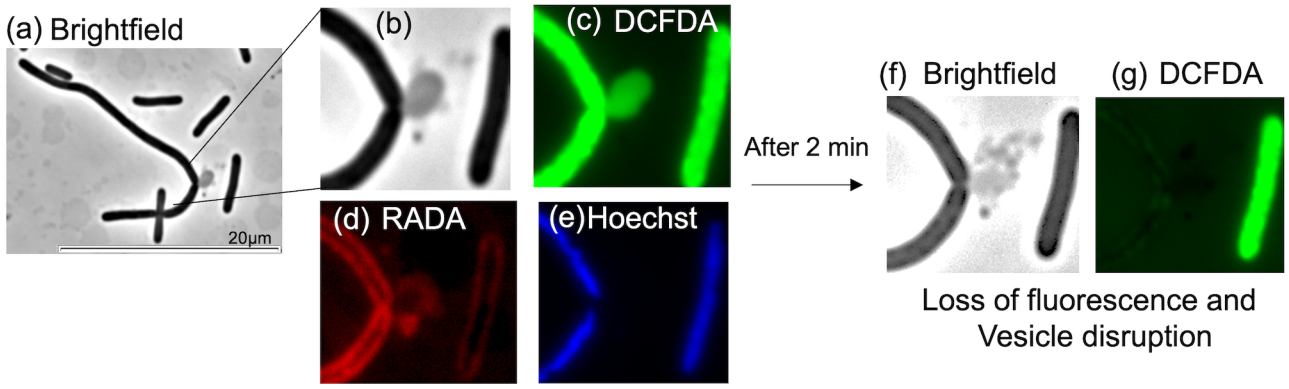
(a) Brightfield
20μm
(b)
(c) DCFDA
(d) RADA
(e)Hoechst
After 2 min
(f) Brightfield
(g) DCFDA
Loss of fluorescence and
Vesicle disruption

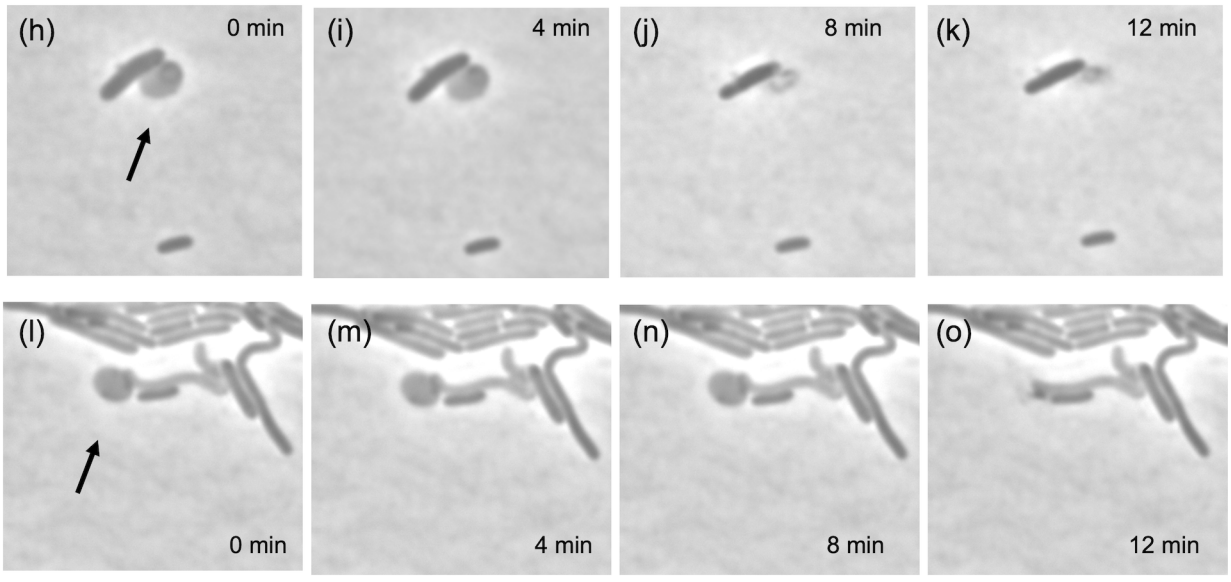
(h) 0 min
(i) 4 min
(j) 8 min
(k) 12 min
(l) 0 min
(m) 4 min
(n) 8 min
(o) 12 min

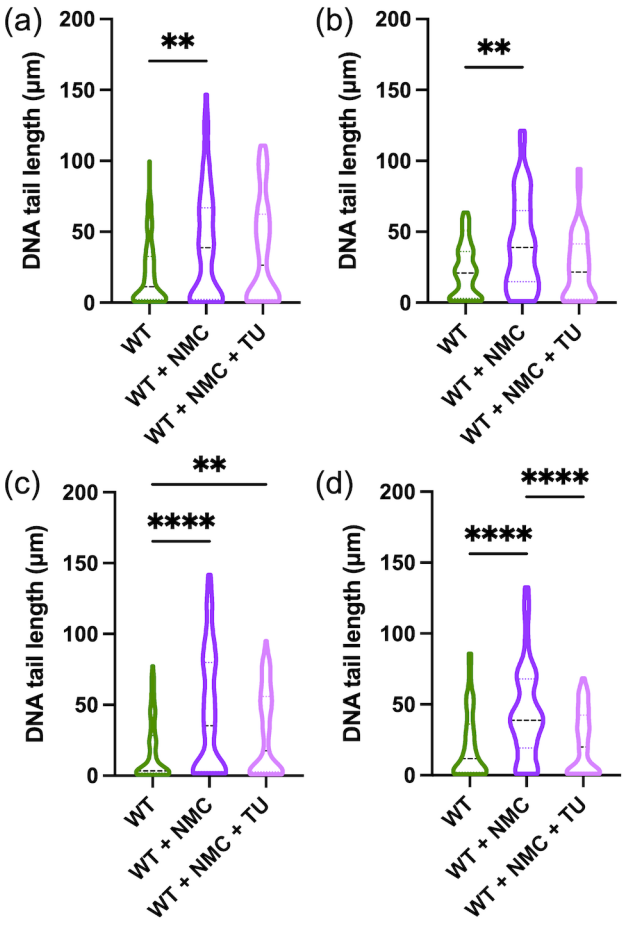
(a)
(b)
(c)
(d)
DNA tail length (µm)
200
150
100
50
0
**
****
WT
WT + NMC
WT + NMC + TU

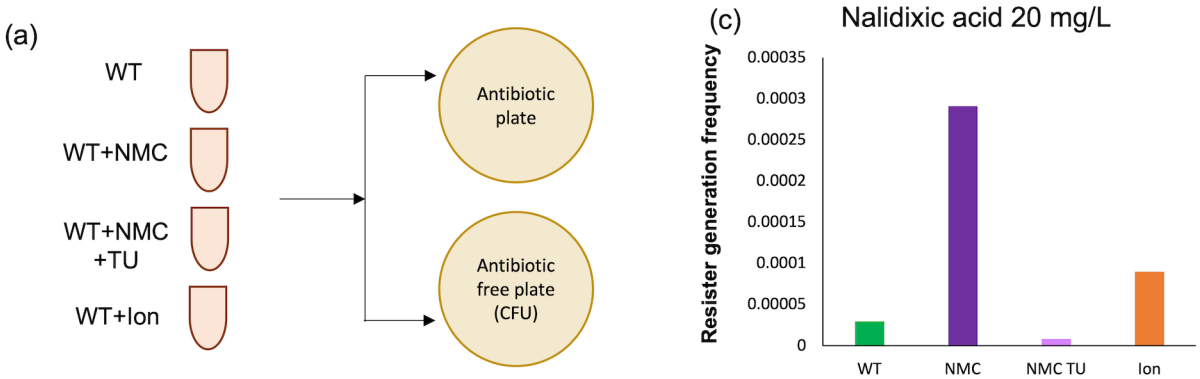

(b)

$$\text{Resister generation frequency} = \frac{\text{Number of colonies on antibiotic containing plate}}{\text{Total number of cells plated (calculated using CFU)}}$$

(d)

```
WT-stock        GGTGACTCGGCGGTATACGATACTATCGTACGTATGGCTCAGCC
WT-pass-D       GGTGACTTGGCGGTATACGATACTATCGTACGTATGGCTCAGCC
NMC1-pass-D     GGTGACTGGGCGGTATACGATACTATCGTACGTATGGCTCAGCC
NMC2-pass-D     GGTGACTTGGCGGTATACGATACTATCGTACGTATGGCTCAGCC
Ion1-pass-D     GGTGACTTGGCGGTATACGATACTATCGTACGTATGGCTCAGCC
Ion2-pass-D     GGTGACTTGGCGGTATACGATACTATCGTACGTATGGCTCAGCC
                ******* ***************************************
```